Modeling Air–Land–Sea Interactions Using the Integrated Regional Model System in Monterey Bay, California

YU-HENG TSENG AND SHOU-HUNG CHIEN

Department of Atmosphere Sciences, National Taiwan University, Taipei, Taiwan

JIMING JIN

Departments of Watershed Sciences and Plants, Soils, and Climate and Utah Climate Center, Utah State University, Logan, Utah

NORMAN L. MILLER

Department of Geography, University of California, Berkeley, and Earth Sciences Division, Lawrence Berkeley National Laboratory, Berkeley, California

(Manuscript received 10 December 2010, in final form 28 October 2011)

ABSTRACT

The air–land–sea interaction in the vicinity of Monterey Bay, California, is simulated and investigated using a new Integrated Regional Model System (I-RMS). This new model realistically resolves coastal processes and submesoscale features that are poorly represented in atmosphere–ocean general circulation models where systematic biases are seen in the long-term model integration. The current I-RMS integrates version 3.1 of the Weather Research and Forecasting Model and version 3.0 of the Community Land Model with an advanced coastal ocean model, based on the nonhydrostatic Monterey Bay Area Regional Ocean Model. The daily land–sea-breeze circulations and the Santa Cruz eddy are fully resolved using high-resolution grids in the coastal margin. In the ocean, coastal upwelling and submesoscale gyres are also well simulated with this version of the coupled I-RMS. Comparison with observations indicates that the high-resolution, improved representation of ocean dynamics in the I-RMS increases the surface moisture flux and the resulting lower-atmospheric water vapor, a primary controlling mechanism for the enhancement of regional coastal fog formation, particularly along the West Coast of the conterminous United States. The I-RMS results show the importance of detailed ocean feedbacks due to coastal upwelling in the marine atmospheric boundary layer.

1. Introduction

Coastal margins are one of the planet's greatest natural resources and economic assets, and they are home to a great diversity of life, including much of the human population. These areas include the Asian Pacific marginal sea regions, the West Coast of the conterminous United States, and many other regions. Yet coastal margins are at the greatest risk due to climate change (e.g., McGranahan et al. 2007; Harvey and Nicholls 2008). Current state-of-the-art atmosphere–ocean general circulation models (AOGCMs) lack sufficient process-level descriptions to adequately capture coastal margin and land–sea interactions (Solomon et al. 2007, chapter 11). Furthermore, AOGCMs do not realistically describe land–sea transition gradients due to their coarse spatial resolution, which produces biases in temperature and other variables. Large and Danabasoglu (2006) attributed major model biases to unresolved air–land–sea interactions within the AOGCMs that are closely associated with coastal upwelling and atmospheric dynamics along the ocean's eastern boundaries.

It is well recognized that AOGCMs cannot provide information at scales finer than their computational grid (typically on the order of 100–300 km) and are unable to resolve land–sea interaction processes at scales typically less than 100 km. The nearshore and coastal dynamics missing from AOGCMs include several atmospheric processes, ocean dynamics, and air–land–sea interactions,

Corresponding author address: Yu-Heng Tseng, Dept. of Atmosphere Sciences, National Taiwan University, No. 1, Sec. 4, Roosevelt Road, Taipei 10617, Taiwan.
E-mail: yhtseng@as.ntu.edu.tw

DOI: 10.1175/MWR-D-10-05071.1

such as the land–sea-breeze (LSB) circulation, coastal upwelling, and submesoscale boundary layer features, among others. The LSB is one of the most common fundamental atmospheric circulations within coastal ocean and large lake regions. Since the LSB is generated through different heating rates of land and seawater masses, it also plays a very important role in air–land–sea interactions. A typical LSB breeze pattern is driven by the diurnal thermal gradient between land and water. It depends mainly on the temperature gradient and results in distinctly different vertical circulation patterns. The sea breeze is initiated when the temperature difference between the land and ocean is sufficiently large. As solar heating starts to intensify during the morning, the corresponding pressure gradient gradually increases. The vertical-scale atmospheric heating may develop from 50 m initially up to 300–1000 m in a fully developed phase during the day. The onset of the sea breeze is usually noticed when wind speed increases, temperature on land decreases, and humidity rises near the surface (Atkinson 1981).

Coastal upwelling zones are among the most productive ocean regions. In the eastern Pacific Ocean, upwelling is driven by northwesterly winds associated with the North Pacific subtropical high pressure system. Coastal upwelling is a dominant physical process that occurs between mid-March and mid-October off the West Coast of the United States (Breaker and Mooers 1986). Land surface heating during the summer can result in a thermal low pressure, with relatively higher pressure over the cooler ocean surface. As the subtropical high migrates north during the spring, coastal upwelling often begins abruptly and is defined as the spring transition. This upwelling intensifies and reaches a maximum typically during June, then starts to weaken in mid-October. With the arrival of the Davidson Current, seasonal coastal upwelling ends, although it may still occur at other times of the year when the winds become favorable for upwelling (Tseng et al. 2005; Tseng and Breaker 2007). Ocean temperatures and nutrient content are significantly affected by coastal upwelling. The delivery of cool, nutrient-rich water to the surface due to coastal upwelling can have a profound effect on oceanic ecosystems, and variations in upwelling can result in large and significant changes in marine productivity and turbulent mixing (Tseng and Ferziger 2001a,b). It is commonly known that coastal upwelling lowers sea surface temperatures (SSTs) and may affect diabatic processes and evaporation in the marine atmospheric boundary layer (MABL).

Researchers have investigated coastal upwelling intensively over the coasts of Oregon, Peru, and northwest Africa due to its importance in marine bioproductivity, fisheries, and climate change (e.g., Smith 1981; Breaker and Mooers 1986; Tseng et al. 2005). However, the actual physical process has not been resolved within the latest AOGCMs largely due to their coarse resolution, which results in a significant warm bias in the open ocean (Solomon et al. 2007, chapter 11). Tseng et al. (2005) simulated the regional circulation along the California coast and found that surface wind forcing and atmospheric conditions play an important role in coastal upwelling and its influence on regional circulation. In particular, the nonhydrostatic effects needed to resolve upwelling dynamics for coastal regions cannot be ignored, because different instability mechanisms and the presence of a density inversion layer are involved (Tseng and Breaker 2007). Active upwelling along the western U.S. coast usually occurs within a narrow band extending 10–25 km offshore (Huyer 1983), and the internal Rossby radius off central California rarely exceeds 10 km. Upwelling dynamics cannot be realistically simulated with hydrostatic models, which produce an instantaneous mixing of an unstable water column, creating a local mixed zone.

The Santa Cruz eddy (SCE) is another shallow cyclonic circulation commonly observed in the summer over Monterey Bay, forming within the MABL below an inversion. Archer et al. (2005) detailed the formation of the SCE over Monterey Bay, California (a 20 km $\times$ 40 km bay located approximately 100 km south of San Francisco Bay). Most vortices along the western U.S. coast form only during unusual weather events, whereas the SCE forms during about 80% of summer days, primarily in July and August. The horizontal extent of SCEs ranges from 10 to 40 km and they have lifetimes on the order of hours. They are smaller than other western U.S. coastal eddies, except for the Gaviota eddy, which occurs near the Santa Barbara Channel. The Gaviota eddy is comparable in size but was recently reclassified as a narrow zone of strong horizontal wind shear, rather than a vortex (Dorman and Winant 2000).

Such submesoscale processes and their feedbacks occurring in coastal regions cannot adequately be simulated with current AOGCMs. Downscaling techniques have commonly been used and represent essential elements of regional climate change impact analyses (Miller et al. 2009). Dynamic downscaling results in regional finescale features using a fine-resolution regional climate model. This implies that the submesoscale dynamics and the associated physical processes are well resolved and represented. However, ocean dynamics are commonly ignored due to their multiscale complexity. The main objective of this paper is to integrate a high-resolution coastal ocean circulation model with an existing regional climate model for a better understanding of upwelling and of air–land–sea interactions. The Integrated Regional Model System (I-RMS) is evaluated with observed data from

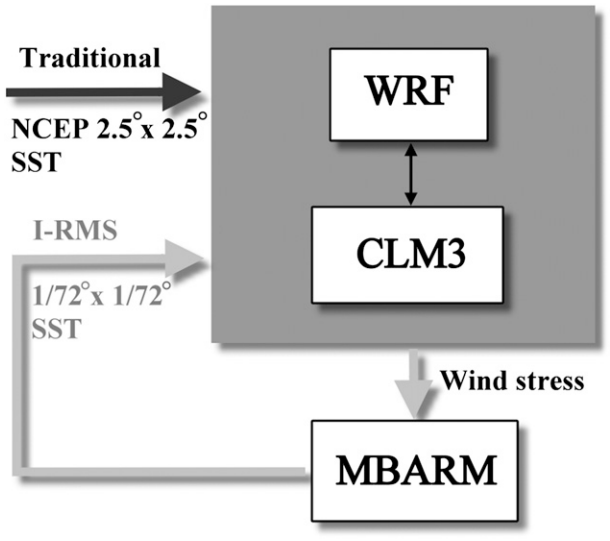

FIG. 1. The structure of the I-RMS.

April 2009. The model development and evaluation shed new light on important nearshore and coastal interface processes for regional weather, and eventually climate studies, including LSB processes, coastal upwelling, and the occurrence of the SCE.

This paper is organized as follows. Section 2 introduces the I-RMS. Section 3 validates nearshore atmospheric and oceanic processes using the April 2009 observations as an example. Section 4 shows the general results in the atmosphere. Section 5 presents the improved I-RMS simulations and the key ocean feedbacks within the air–sea marine boundary layer. Section 6 provides further studies of the model sensitivity to SST forcing on the I-RMS. Finally, conclusions are provided in section 7.

2. Integrated Regional System Model (I-RMS)

We illustrate the I-RMS framework to investigate the physical processes for regional climate modeling in Fig. 1. The I-RMS is derived from version 3.1 of the Weather Research and Forecasting Model (WRF) coupled with version 3.0 of the Community Land Model (WRF-CLM) (Jin et al. 2010). Both WRF and CLM were developed at the National Center for Atmospheric Research (NCAR). In this study, WRF-CLM is integrated with a nonhydrostatic coastal ocean model, the Monterey Bay Area Regional Model (MBARM). The individual model components are introduced briefly in the following subsections.

a. Weather Research and Forecasting Model 3.1 with Community Land Model 3.0 (WRF-CLM)

WRF-CLM is designed as a regional weather and climate model (Skamarock et al. 2005; Skamarock and Klemp 2008) coupled with the Community Land Model (Oleson et al. 2004), a land surface model used in the Community Climate System Model (CCSM). The CLM includes a sophisticated subgrid representation, advanced snow processes, vegetation with plant functional types, and lateral hydrologic flow capability. This coupled system significantly improves land surface process simulations with the WRF model (Jin et al. 2010; Miller et al. 2009).

The atmospheric component of WRF-CLM solves the equations of motion using fully compressible, Euler nonhydrostatic Navier–Stokes equations, where the scalar variables are conservative. The horizontal grid uses the staggered Arakawa C grid, while the vertical grid uses a terrain-following hydrostatic-pressure vertical coordinate. The model top is set at 50 hPa in our simulations. Four nested domains have been configured in our simulations (see Fig. 2a for the covered regions). These four domains are one-way nested at 40.5-, 13.5-, 4.5-, and 1.5-km horizontal resolution, and the corresponding domain dimensions are 50×50, 73×82, 100×142, and 181×160, respectively. The time steps are 216, 72, 24, and 8 s, respectively. Lateral boundary conditions are obtained from their parent domains, except for the coarsest domain, which is forced with the National Centers for Environmental Prediction (NCEP)–NCAR $2.5° \times 2.5°$ reanalysis data (Kistler et al. 2001). All domains share the same vertical structure of 23 layers, where more than 15 layers are used to resolve the atmospheric boundary layer. The finest domain covers the region 35.76°–37.73°N and 123.20°–120.41°W. Figure 2b shows the terrain from the finest-resolution domain used in the WRF-CLM. The solid line is a vertical section along the Moss Landing River, and the dashed line is a vertical section along the Salinas Valley. All observational stations used in this study are shown in Fig. 2b, including 11 meteorological stations, 2 ocean surface mooring stations [46092 (M1) and 46042 (M2)], and 1 buoy station (46236).

b. Monterey Bay Area Regional Model

Since the ocean SSTs used in the WRF-CLM were interpolated using the 6-h, $2.5° \times 2.5°$ resolution NCEP–NCAR reanalysis data, the model cannot accurately account for the detailed influence of coastal upwelling or ocean-driven processes (e.g., coastal fog formation) due to the resolution constraint. Coarse-resolution SST forcing likely results in misinterpreted submesoscale air–land–sea interaction processes for long-term climate integration. In particular, the frequent fog formation in Monterey Bay resulting from coastal upwelling is very sensitive to the spatial and temporal variations of SSTs. Hence, to accurately represent regional air–land–sea interactions in the vicinity of Monterey Bay, we coupled the WRF-CLM with a nonhydrostatic, z-level, mixed

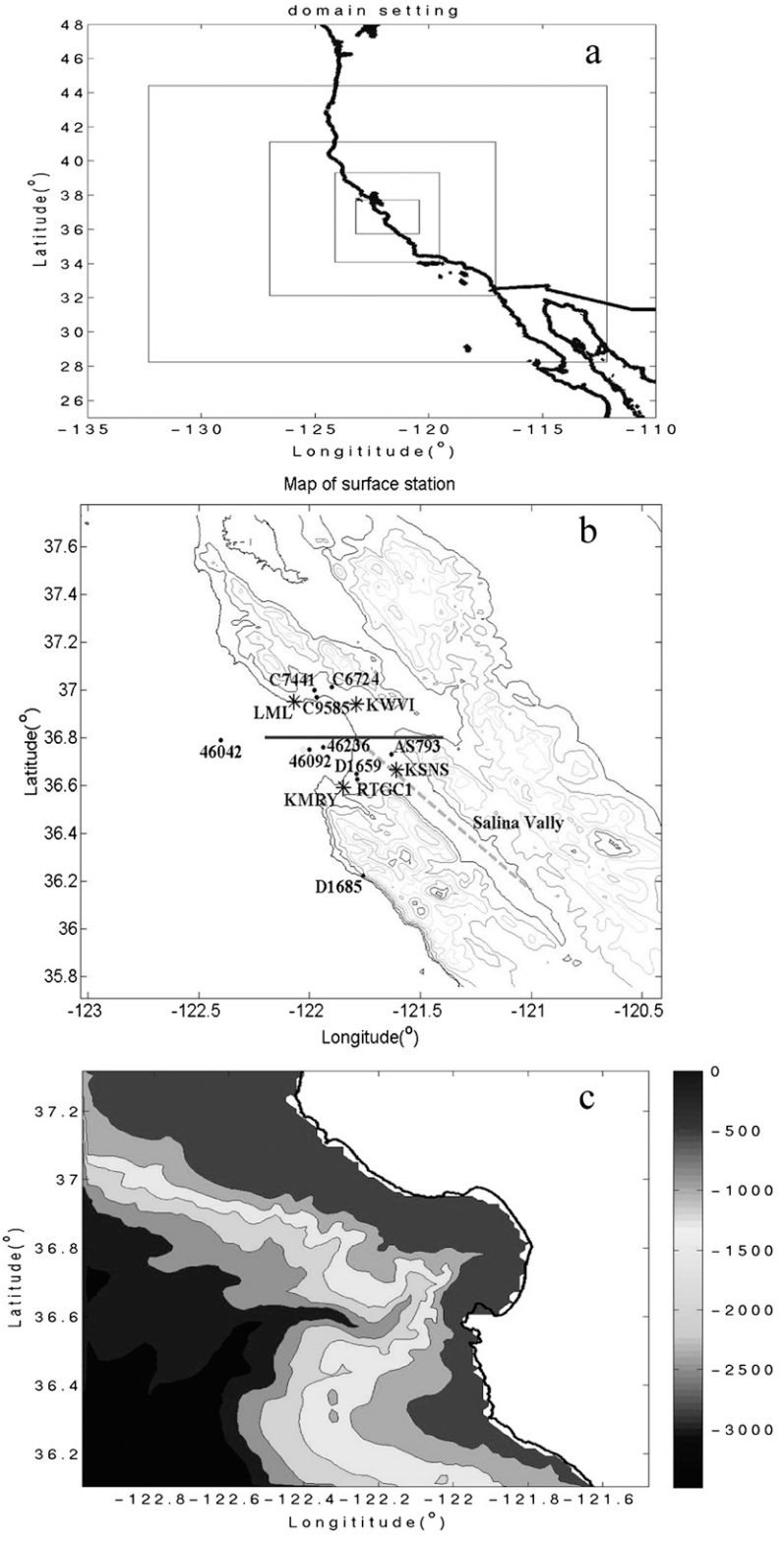

FIG. 2. (a) The four-level nested domain of the I-RMS. (b) The land terrain used in the I-RMS and the observational stations used in this study (dots are from NWS while asterisks are from MesoWest). (c) The bathymetry used in the coastal ocean model. Note that the Monterey Submarine Canyon is clear.

Arakawa A and C grid, fourth-order accurate version of MBARM (Tseng et al. 2005; Tseng and Breaker 2007). The MBARM is a high-resolution coastal ocean model in which the dynamics are determined by the complex coastline and steep topography. It is also one-way coupled to a large-scale California Current System (CCS) model (Tseng et al. 2005; Tseng and Breaker 2007). Bathymetry is from unfiltered U.S. Geological Survey 250-m-resolution topography data (Wong and Eittreim 2001) and is presented in Fig. 2c.

The domain of the MBARM covers from 36.05°N to 37.37°N and 121.41°W to 123.06°W (Fig. 2c), and the horizontal spatial resolution is $^1/_{72}$° (1.5 km). The vertical grid has 28 nonuniformly spaced levels; see Tseng et al. (2005) for a more detailed model description. The deepest ocean level is more than 3000 m, significantly greater than the maximum land terrain elevation for this region, where the highest mountain peak is 1400 m. The wind stress originally came from the 1° × 1° monthly climatology of Hellerman and Rosenstein (1983), but the I-RMS internally generated surface wind field is used here instead.

c. The I-RMS settings

In the coupled I-RMS, the momentum flux is transferred from the atmosphere to the ocean by the wind stress, while the modeled SSTs are used to force the atmospheric component. The surface wind stress in the I-RMS was derived from a modified drag coefficient formulation (Stewart 2008). The NCEP 6-hourly SSTs in the WRF-CLM component were replaced by the modeled SSTs from the MBARM component. Simulations of the I-RMS begin with a WRF-CLM integration, which provides an update to the MBARM upper-boundary forcing for the entire study period. Subsequently, the output of the MBARM is then used to force the WRF-CLM at its lower sea surface boundary at each time step. The resolved SSTs include more accurate boundary forcing for the I-RMS, providing potentially significant improvements to the modeling of nearshore processes and atmospheric dynamics. Note that the WRF-CLM needs to be run twice here. The I-RMS modeling approach described above is an effective way of investigating the interactions between the atmosphere and ocean surface before our next step in the two-way coupled modeling system is developed and evaluated.

Three different numerical experiments have been conducted in this study (Table 1). The first experiment is the WRF-CLM simulation, which is driven by the default NCEP–NCAR reanalysis 6-hourly SST forcing. This experiment is used to verify whether such traditional regional climate models can appropriately simulate the nearshore processes at fine resolution. The second experiment is the I-RMS simulation, where the MBARM is integrated with the WRF-CLM. The last numerical experiment is identical to the WRF-CLM simulation, except its bottom boundary is forced by the NCEP–NCAR reanalysis 6-hourly SST with a uniform 0.6°C increase within the model domain (hereafter WRF-CLM$_{plus}$). This experiment is performed to examine the sensitivity of the WRF-CLM to SSTs since the mean SST of the I-RMS is roughly 0.6°C higher than that of the WRF-CLM over the whole simulation period (Fig. 3). This value is slightly larger than the standard deviation of the SST (0.46°C) used in the WRF-CLM simulation and is a reasonable estimation. Therefore, the additional WRF-CLM$_{plus}$ experiment is designed to further examine the influence of SST. Other SST forcing sensitivity indicates that a quasi-linear relationship can be found in the response of moisture flux, surface temperature, and others. The initial and 6-h updated lateral boundary conditions in the WRF-CLM and WRF-CLM$_{plus}$ simulations are both taken from NCEP–NCAR reanalysis 2.5° × 2.5° data. In general, these experiments differ only in terms of their spatial SST distributions.

TABLE 1. Numerical experiments.

Expt	Boundary forcing for the atmospheric models
WRF-CLM	SST from NCEP–NCAR 6-hourly data
I-RMS	SST from MBARM
WRF-CLM$_{plus}$	SST 2°C higher than NCEP–NCAR 6-hourly data everywhere

Each experiment is set up for a 10-day simulation, from 1700 local standard time (LST) 10 April to 1700 LST 20 April. The WRF-CLM is spun up for an initial 24 h for each experiment, and the model output from the spinup period is discarded. An 8-yr spinup run with the MBARM from rest is performed, where it is seen that the equilibrium state for April is reached (Tseng et al. 2005).

3. Observations and model validation

The North Pacific high is the dominant feature off the California coast during late spring to fall, contributing to a sea–land pressure gradient that drives persistent anticyclonic north-northwesterly winds over the California and Oregon coasts. Climatologically, the surface wind stress and wind stress curl are consistently favorable for upwelling between April and October. The positive wind stress curl can be extended several hundred kilometers offshore from central California, and coastal upwelling (and associated Ekman pumping) commonly occurs during this period. Thus, it is well known that spring and summer are the typical upwelling seasons in Monterey

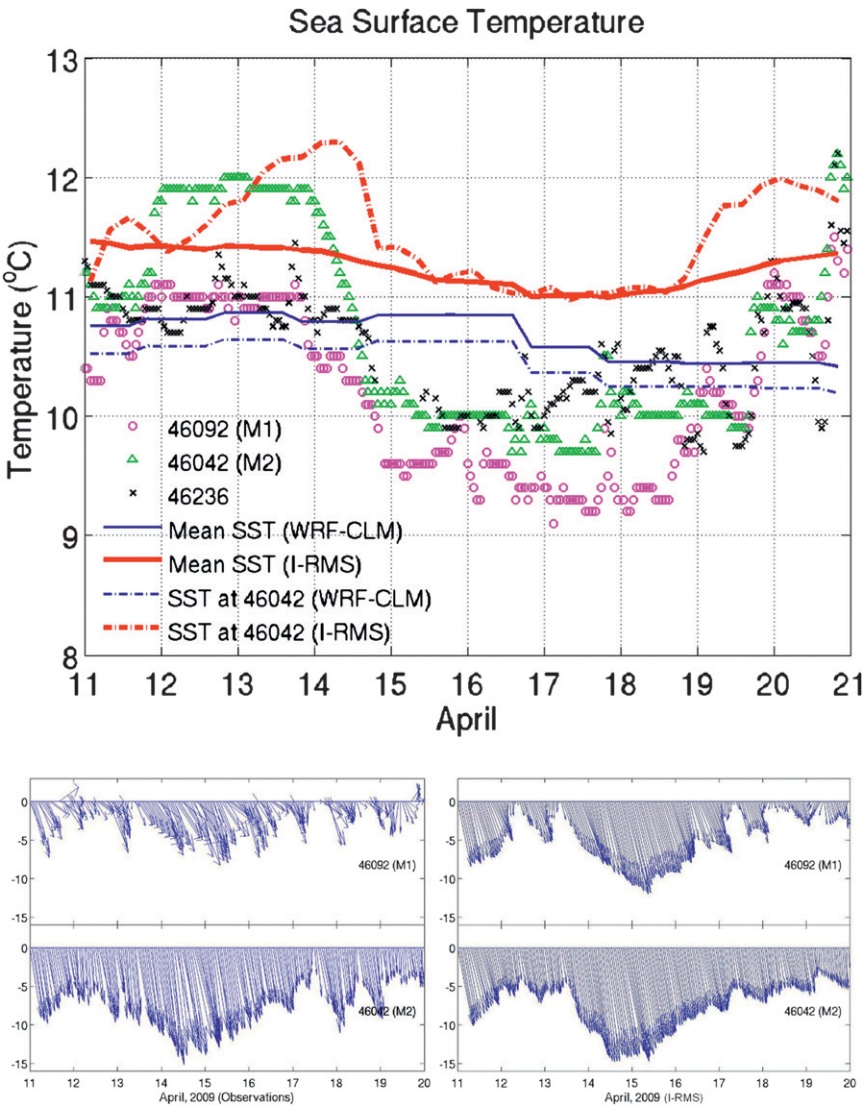

FIG. 3. (top) Comparison of the mean SST for the finest domain and the SST near mooring 46042 (M2) for the WRF-CLM and the I-RMS simulations, respectively. The mean SST for the I-RMS is generally higher than that for the WRF-CLM. The I-RMS uses a more realistic SST distribution both in time and space. This should result in a more accurate representation of nearshore processes. The SST observations from the three ocean surface measurements are also shown. (bottom) The time series of observed wind directions and speeds for the 46092 (M1) and 46042 (M2) stations in the I-RMS. See the map in Fig. 2b for their locations.

Bay. The temperature is about 4°C lower than that at comparable latitudes in the open Pacific Ocean (Johnstone and Dawson 2010). In the following, we use the April 2009 observations to analyze atmospheric and oceanic processes off the California coast.

a. Station information

Fourteen stations were selected from the National Weather Service (NWS) and MesoWest weather surface dataset (http://mesowest.utah.edu), which provides high quality observed surface wind fields with hourly temporal resolution. Figure 2b includes the locations of these meteorological stations. Buoy stations M1 (46092) and M2 (46042) were two ocean mooring stations where surface wind measurements exist in the vicinity of Monterey Bay. Note that wind observations from M1 and M2 show the common prevailing northwesterlies in Monterey Bay; this is because their locations are not affected by the land terrain. Stations such as Long Marine Laboratory (LML), Monterey Peninsula Airport (KMRY),

TABLE 2. Correlation with the observation for WRF-CLM and I-RMS.

	SST		SLP		Wind speed	
Station	WRF-CLM	I-RMS	WRF-CLM	I-RMS	WRF-CLM	I-RMS
M1	0.36	0.70	0.94	0.94	0.87	0.87
M2	0.43	0.67	0.95	0.95	0.86	0.88

Salinas Municipal Airport (KSNS), and Watsonville Municipal Airport (KWVI) usually indicate strong upwelling favorable winds (UFWs) from April to August. These stations are also representative for SCE and LSB circulation patterns. The other stations, Santa Cruz (C7441 and C9585) and Aptos (C6724), are located north of Monterey Bay, where the sea-breeze circulation may differ in orientation from the other four stations during the same period.

b. *Atmospheric winds*

Validation of the current I-RMS is critical for detailed modeling of air–land–sea interactions in the vicinity of Monterey Bay. The period from 11 to 20 April 2009 was selected here for such validation and further analysis. The model grid points that are closest to the observation locations are chosen for the analysis. The performance of both the WRF-CLM and the I-RMS against observations at two mooring stations is summarized in Table 2. Both simulations show high correlation (larger than 0.86) with the observed wind speeds and sea level pressure (SLP), but only the I-RMS also exhibits a high correlation for SST (discussed later). The good performance with respect to winds is further supported by the comparison of wind direction and speed at the two mooring stations, M1 and M2 (bottom panel of Fig. 3), as well as at seven other stations (Fig. 4a) at which observed data were completed during the simulation period. Outside the bay (M2 station), both simulations and observations show northwesterly wind fields, while within the bay (M1 station), observations show a more variable wind field due to the complex topographic influence upstream. However, the major wind direction is generally northwesterly. In general, the difference between the modeled atmospheric dynamics with the WRF-CLM and I-RMS were not significant within the short simulation time in this study. Thus, only I-RMS wind results are shown in the rest of this section.

Table 3 indicates the corresponding correlations between the I-RMS results and observations at these stations. The I-RMS results at all stations correlate very well on surface temperature, surface pressure, and wind speed except for the KMRY station (see Fig. 2 for location). The discrepancy is not surprising because this local airport station is very close to the city of Monterey, and the land use and local topography may significantly affect wind speed, as the resolution is not enough to resolve the urban canopy.

Archer et al. (2005) reported that the SCE, a commonly observed submesoscale phenomenon, occurred twice almost every night in the summer. The SCE is observed during our study period; however, it seems to appear only once a night. This may be because the diurnal temperature difference is smaller in spring than in summer, as observed by Archer et al. (2005). The SCE signals are found almost every night (Fig. 4a). For example, from the station RTGC1, we can see that a southwesterly/southerly wind appears almost every night except 14 and 15 April, which may be related to the strengthening of UFWs. Figure 5a illustrates a typical SCE pattern that forms at night based on the geographically scattered stations. The sketched arrow in Fig. 5a indicates the wind field pattern. A cyclonic wind field occurs from 1700 LST 16 April until 1000 LST 17 April. Model results show a similar pattern that lasts for a shorter period than the observations.

The LSB circulation is also accurately simulated with the I-RMS (cf. Figs. 4a and 4b). It is of interest to note that the sea-breeze pattern is more frequent than the land-breeze pattern. The sea-breeze pattern is found almost every afternoon; for example, southerlies frequently occur at C7441, C9585, and KWVI in the afternoon while the land-breeze pattern is relatively weak and rarely occurs. Figure 5b shows a typical strong sea-breeze pattern is established during the afternoon of 18 April. A weak land-breeze pattern appears in the morning (Fig. 5c). This is not surprising since a strong synoptic-scale prevailing wind is often dominant in the spring. Overall, the modeled LSB is quite consistent with observations (Fig. 4).

The prevailing UFW pattern is commonly seen along the California coast from early spring to late summer. The time period from 14 to 16 April 2009 shows such an example. The maximum wind speed at these stations is generally near 12 m s^{-1}, except during the UFW period, when it can reach 15 m s^{-1}. The strong UFW may weaken the strength of the SCE and LSB (Fig. 4). Figure 5d shows a typical observed spatial distribution of UFW. The UFW can last for a few days, resulting in the typical coastal upwelling found in Monterey Bay (Tseng et al. 2005; Tseng and Breaker 2007). A significant SST decrease of up to 2°C is seen during the UFW period (Fig. 3), where a strong prevailing wind is observed almost exclusively during the daytime hours. The modeled UFW is quite clear at all stations. However, the modeled UFW is much stronger at most stations than in the observations due to the weakened influence of the complex land terrain on the wind field in the model compared to

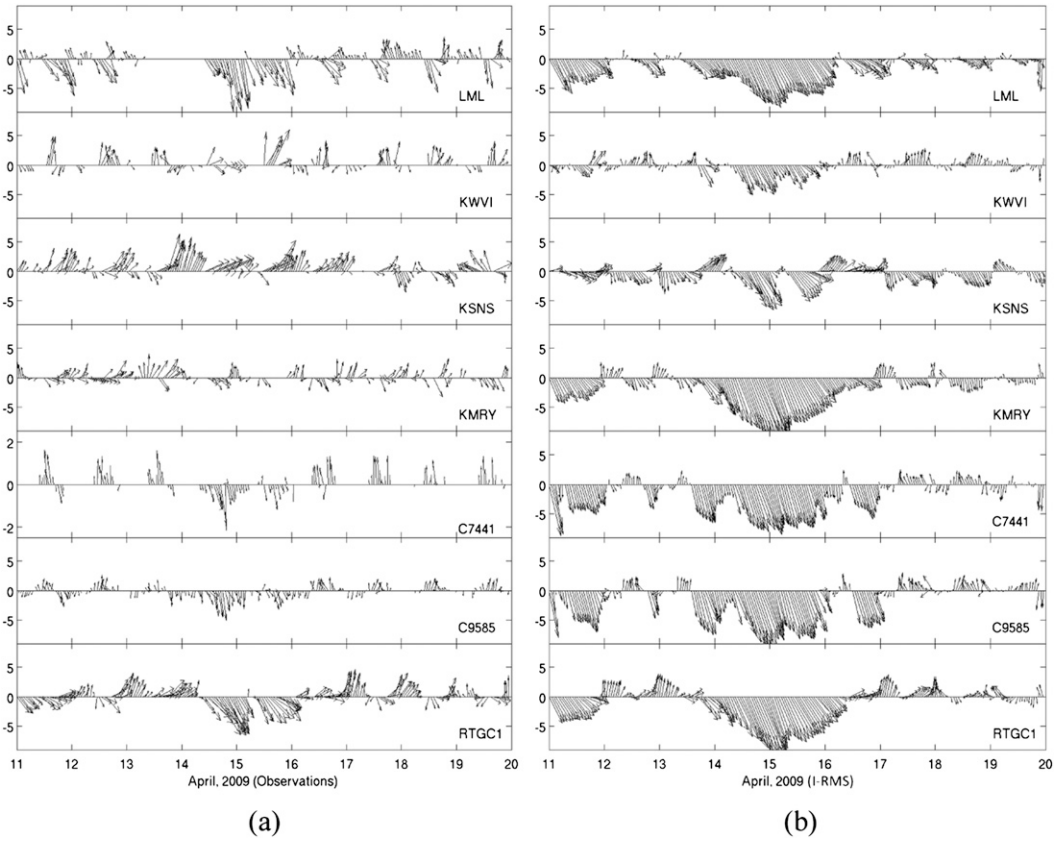

FIG. 4. (a) The time series of observed wind direction and speed for seven stations, where data are more complete over the simulation period. (b) The time series of modeled wind directions and speeds in the I-RMS for the same stations shown in (a). (c) The time series comparison of the observed and modeled temperatures (I-RMS) for the same stations shown in (a): T_s, surface temperature; T_d, dewpoint temperature.

the actual processes. As expected, the 1.5-km resolution model produces more persistent patterns in the UFW than do the observations.

In general, the I-RMS accurately captures the observed wind patterns for different events. This confirms that the high-resolution I-RMS can reproduce the major submesoscale circulation pattern that cannot be resolved in AOGCMs. The realistic simulations of these circulations can lead to a better understanding of the key air–land–sea dynamics over coastal areas, which is further discussed in section 4.

c. Temperature and humidity

Whereas the correlation of the two model systems with observations is high for winds and SLP, the correlations of SST from Table 2 are only 0.36–0.43 for the WRF-CLM and 0.67–0.7 for the I-RMS. The major difference between these two simulations is the spatial distribution of SSTs and their associated surface flux. Figure 3 shows the spatially mean SSTs for the 1.5-km-resolution domain and the SSTs near mooring 46042 (M2) for the WRF-CLM and the I-RMS simulations, respectively. The I-RMS uses a more detailed SST distribution produced with the MBARM at 1.5-km resolution, while the WRF-CLM uses the 2.5° × 2.5° NCEP–NCAR reanalysis SST data. Thus, it is expected that nearshore processes could be more accurately resolved with the I-RMS, and how such processes affect air–sea flux exchanges is delineated through comparison of these experiments (discussed in later sections).

The observed SSTs at three different locations during the simulation period are also shown in the top panel of Fig. 3. Here, a 1°–2°C decrease is seen after the onset of the UFW on 13–14 April (see also the wind direction and speed in the bottom panel of Fig. 3). The SST used to force the I-RMS shows a sudden decrease of 1°–1.5°C within a few hours (Fig. 3a). However, the mean SST for the WRF-CLM originally is approximately 1°C cooler than that for the I-RMS and starts to decrease after 15 April. This is not surprising, because the WRF-CLM SSTs derived from the NCEP–NCAR data are distributed more homogeneously, and thus, a significant change near

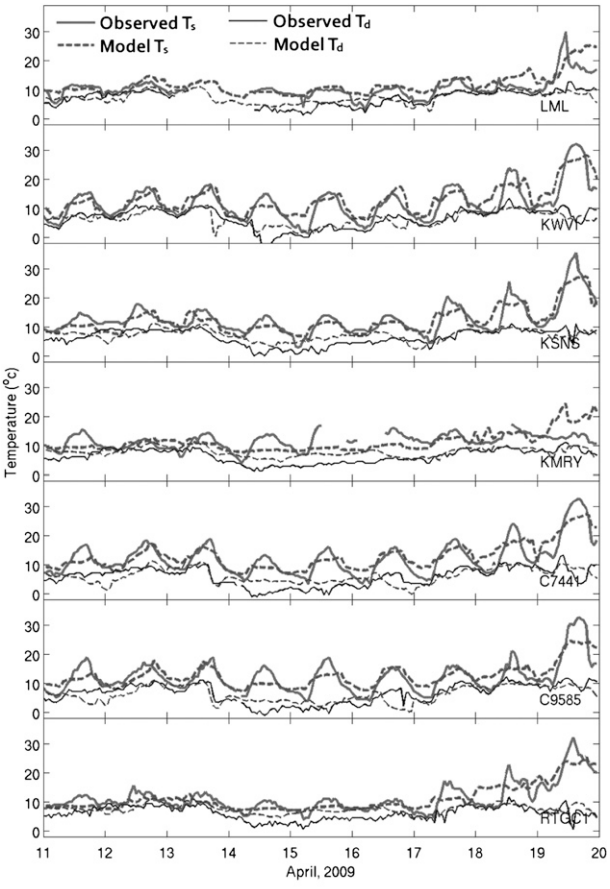

(c)

FIG. 4. (*Continued*)

station 46042 (M2) cannot be shown (Fig. 3). The SST in the I-RMS near the same station decreases by approximately 1.2°C, closer to the observed decrease (~2°C), while the SST for the WRF-CLM decreases by only 0.3°C overall on 15 April. This indicates that the influence of coastal upwelling may be markedly underestimated in the original version of the WRF-CLM due to the poor quality of the SST forcing data derived from the NCEP–NCAR reanalysis data. Although the general SST pattern is captured by the I-RMS, discrepancies still exist, which most likely result from the uncertainty of the initial and/or lateral boundary conditions. Comparison of surface temperature T_s and dewpoint temperature T_d between the I-RMS simulations and observations is also shown in Fig. 4c. The diurnal cycles of temperature and humidity are also reasonably represented in the I-RMS (e.g., Table 2).

4. General results in the atmosphere

The WRF-CLM code has been developed and used for regional climate modeling (Jin et al. 2010; Miller et al. 2009). However, the WRF-CLM, like all other regional climate models, requires sufficiently adequate lateral boundary conditions to maintain the elements of synoptic- and large-scale circulation patterns (Cui et al. 1998). The 1.5-km-resolution WRF-CLM simulation is expected to produce reasonable synoptic-scale patterns that resolve submesoscale circulations within our study area. Because of the similarities in the atmospheric dynamics simulated with the WRF-CLM and I-RMS, discussed previously, results in this section will focus on the WRF-CLM.

TABLE 3. Correlation between the model and observations from seven individual stations.

Station	Surface temperature	Surface pressure	Wind speed
LML	0.75	0.91	0.56
KWVI	0.84	0.93	0.61
KSNS	0.85	0.93	0.61
KMRY	0.31	0.94	0.04
C7441	0.85	N/A	0.35
C9585	0.83	N/A	0.51
RTGC1	0.82	N/A	0.70

a. LSB circulation

It is commonly known that the sea-breeze circulation cell begins near the coast in the morning and expands landward as land surface heating increases. The expansion is not symmetric with respect to the coastline; it is significantly greater over the water due to the difference in thermal heating intensity. Haurwitz (1947) indicated that as the sea breeze becomes stronger, the temperature gradient, a sea-breeze driver, is reduced. Figure 6a shows the modeled sea-breeze pattern that develops in the afternoon overlaid with the land topography of the Salinas Valley (see Fig. 2b for the local map). The model produces a late afternoon sea-breeze event where a landward, along-valley wind develops. During a morning land breeze, a seaward, along-valley wind is found (Fig. 6b). This LSB circulation is one of the most important nearshore physical phenomena. In the Salinas Valley, the along-valley land breeze is usually weaker than the sea breeze, likely due to the prevailing synoptic wind flowing into the valley mouth.

Figures 6c and 6d further show the temperature and wind field of the LSB near the bay and offshore regions (also see the local map in Fig. 2b). The sea-breeze circulation occurs near the mouth of Monterey Bay (Fig. 6c) and is associated with the strong temperature gradient. An onshore wind can be seen almost every afternoon in the simulations. Figure 6d clearly shows a land-breeze circulation pattern occurring mostly in the mornings, and a seaward land breeze can be seen in all coastal areas inside Monterey Bay.

Banta (1995) indicated that the height of the LSB circulation was normally below 1500 m and was located

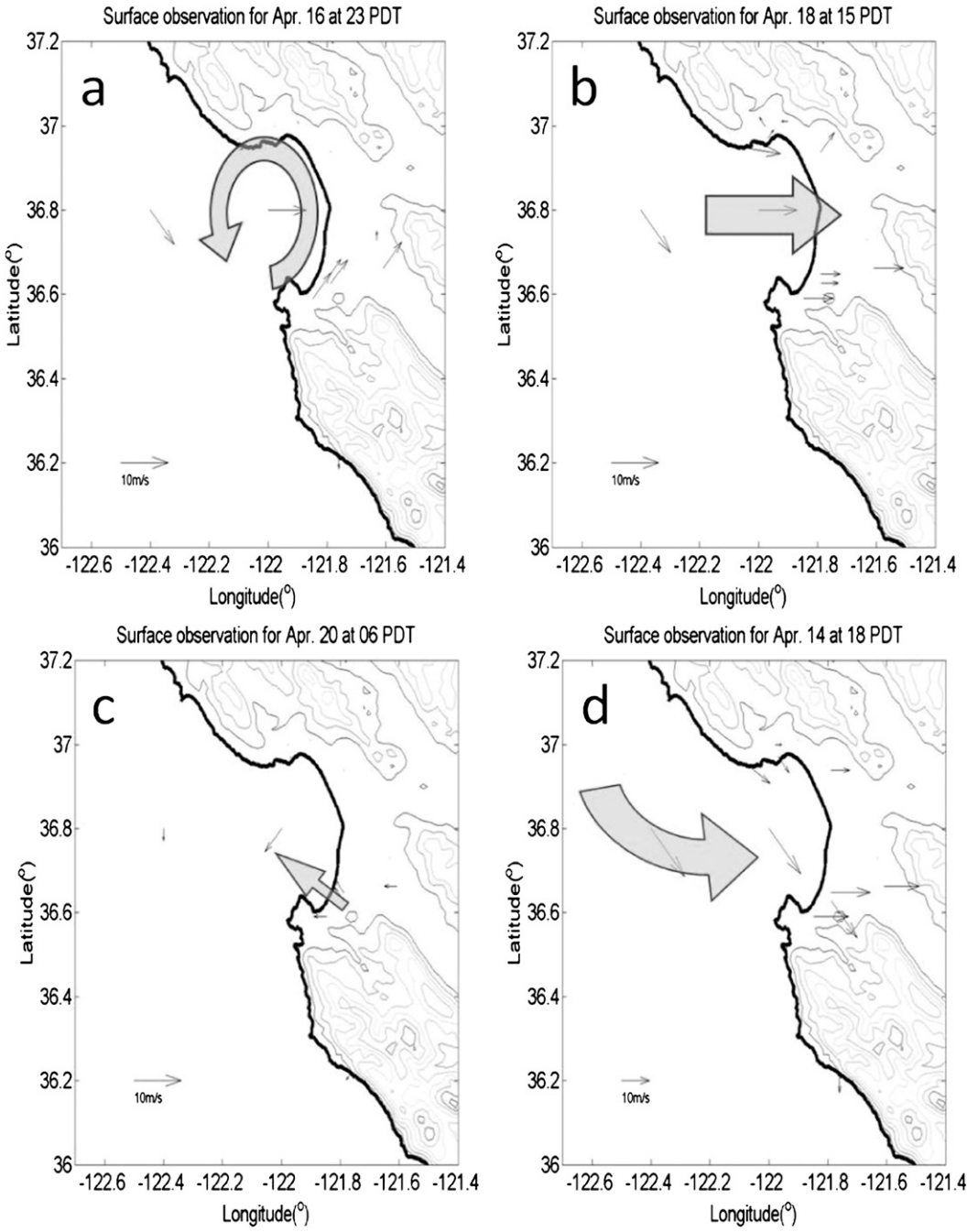

FIG. 5. (a) A typical SCE pattern that forms from the observations. (b) A typical sea-breeze pattern established in the afternoon. (c) A weak observed land-breeze pattern in the morning. (d) A typical spatial distribution of UFW from the observations. The observational wind fields are shown, with both direction and speed included.

at less than 300–1000 m above sea level. Figure 7a shows the wind field (black arrows) of the typical sea breeze along a vertical section in the Moss Landing area (solid line in Fig. 2b). The corresponding potential temperature is superimposed (the contour interval is 1 K). The return flow in the upper level was lower than 1000 m. Over the northern California coast, the temperature inversion typically occurs at elevations of 400–500 m and is considerably lower than that in other regions. Inland penetration of marine air is thus limited to the coastal zone at a low elevation, with an interior boundary defined by the temperature inversion height and the local

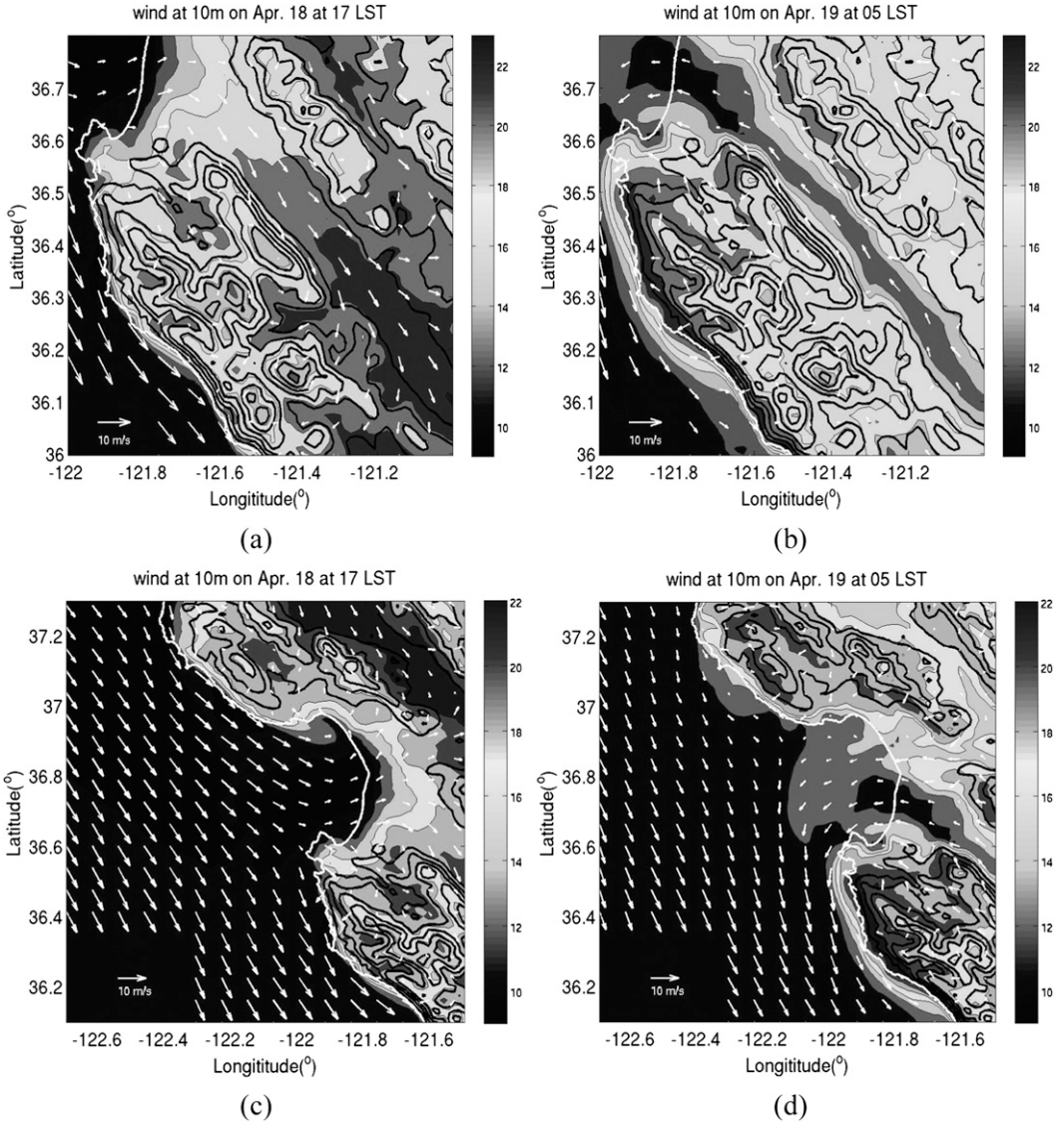

FIG. 6. The modeled LSB circulation overlaid with terrain elevation (black contours every 200 m) in WRF-CLM. The temperature at the lowest level is shaded and the 10-m wind field is shown as vectors. The modeled (a) sea- and (b) land-breeze circulations in the Salinas Valley and the simulated (c) sea- and (d) land-breeze circulations near the bay mouth and offshore regions.

relief (Johnstone and Dawson 2010). Our simulation indicates that the LSB circulation initiated from the upper portion of the atmospheric boundary layer ends when the wind signal approaches zero near the land surface. Neither convergence nor divergence can be found in the vertical cross section. The potential temperature profile shows relatively stable vertical temperature stratification, as compared to a weak stratification within the Salinas Valley; Lyons (1972) reported a similar occurrence. Mostly, the boundary layer wind fields show a consistent onshore northwesterly wind, but only limited return (offshore) flow is seen while a sea breeze occurs. The atmospheric boundary layer in these areas is conducive to the development of low-level stratocumulus clouds that often form just below the inversion base and typically lie several hundred meters above the sea surface (Johnstone and Dawson 2010).

Figure 7c shows the modeled eastward and northward wind speeds from 12 to 20 April near the M1 mooring (black spot in Fig. 2b) with the WRF-CLM. The wind field shows a typical pattern over this area (e.g., Vesecky et al. 1997). A diurnal cycle is clearly seen in both wind directions, where the eastward wind is generally less than 9 m s^{-1}, except during the UFW event. The maximum

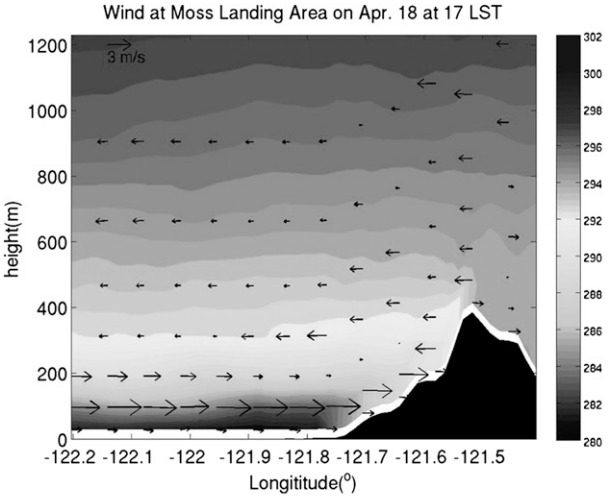

(a)

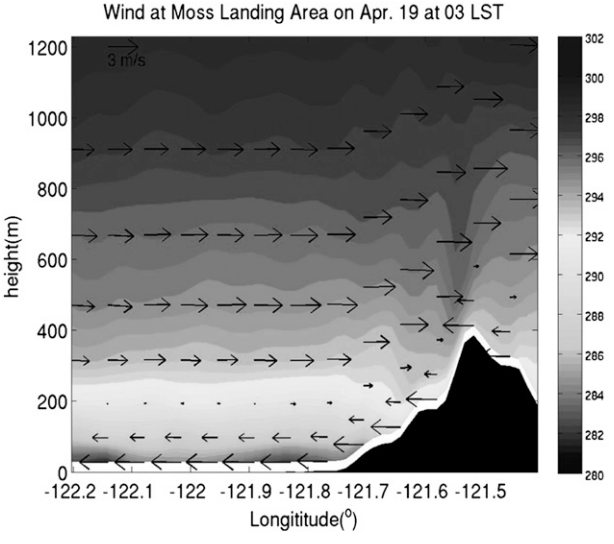

(b)

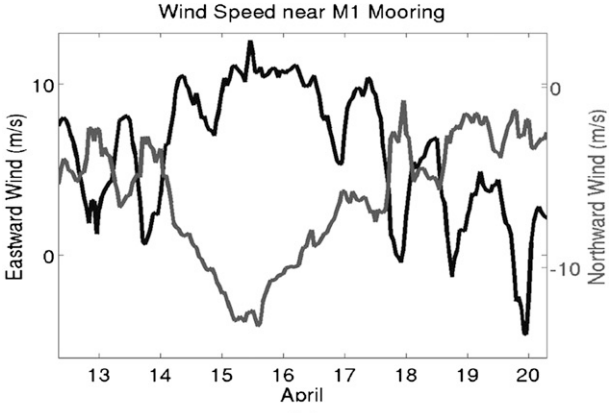

(c)

eastward wind speed occurs in the morning, while a reversed wind (land breeze) is seen mostly at night.

b. The SCE

Similar to the LSB circulation, the SCE is found almost every night in our simulations, except during the strong UFW event. Archer et al. (2005) noted that two SCE events typically occur every night in the summer. However, observations and the high-resolution WRF-CLM simulations for April indicate there may be only one SCE event during spring 2009. After the sea breeze relaxes, the west-northwesterly wind may change into a southerly wind and form a hooklike wind field. This quickly establishes a small eddy that is limited to the northern part of Monterey Bay near KWVI (Fig. 8a). The SCE is then enhanced and develops into a larger eddy, as shown in Fig. 8b. Finally, the eddy dissipates in the early morning and the next sea-breeze circulation system starts to form. Previous studies indicate that the SCE formation requires several mechanisms acting concurrently (e.g., Archer et al. 2005; Archer and Jacobson 2005). These mechanisms include the baroclinic feedback with a solenoidal term, a bottom-friction-generating vorticity, the sea-breeze field, and in the afternoon a flow reversal against the main northwesterly winds created by the meridional pressure gradient. The formation of the SCE is also controlled by the local topography of Monterey Bay, and hence it takes place almost every night.

Our simulation confirms the results of Archer and Jacobson (2005) for the friction generated by the terrain and the sea-breeze field inside Monterey Bay. Figure 9 shows the modeled vertical vorticity from the wind field at a height of 10 m above the surface in the WRF-CLM. The vertical vorticity on the morning of 17 April (Fig. 9a) shows that positive vorticity is formed along the coast to the north of the entrance to the bay, which may be due to horizontal wind shear over the land and ocean, friction against the Santa Cruz Mountains, and flow convergence due to the blocking effect of the mountains (Archer and Jacobson 2005). This is usually associated with the westerly sea breeze in Monterey Bay, while the prevailing wind outside the bay is northwesterly and parallel to the coast. Thus, the surface wind turns from northwesterly at the entrance of the bay to southerly

←

FIG. 7. The wind vector of the typical (a) sea and (b) land breezes along a vertical section in the Moss Landing area (solid line in Fig. 2b). The potential temperature field is shaded. (c) The modeled longitudinal and latitudinal wind speeds during 12–20 Apr near the M1 mooring for the WRF-CLM.

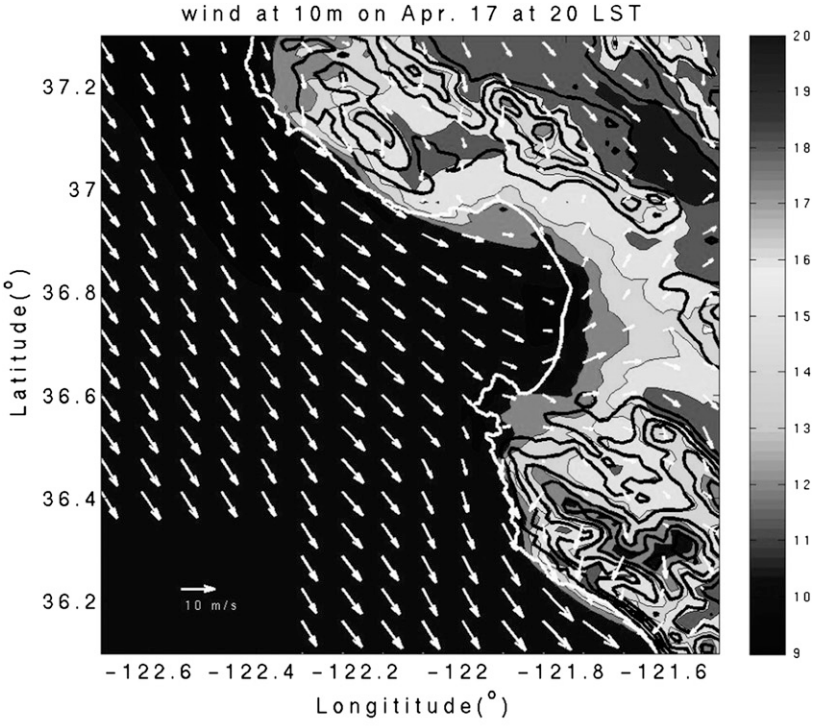

(a)

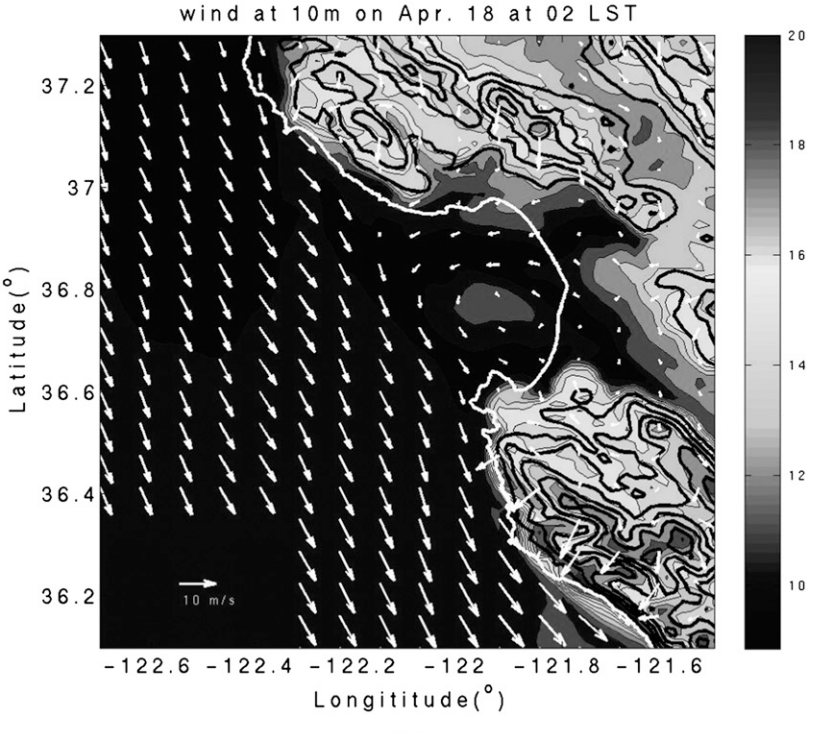

(b)

FIG. 8. The modeled 10-m wind field in the WRF-CLM, overlaid with terrain elevation (black contours every 200 m), showing the formation of the SCE. The temperature at the lowest level is color shaded. The 10-m wind field at (a) 2000 LST 17 Apr and (b) 0200 LST 18 Apr.

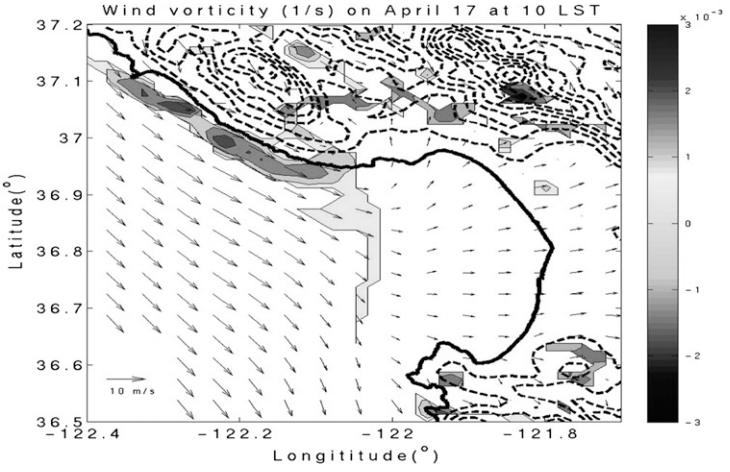

FIG. 9. The modeled 10-m wind field (above the terrain) in the WRF-CLM superimposed over the shaded vertical vorticity (only the strength larger than $|5 \times 10^{-4}|$ s^{-1} is shown). The terrain is shown as the dashed contours (every 200 m is shown) for (a) 1000 LST 17 Apr, (b) 2000 LST 17 Apr, and (c) 0200 LST 18 Apr, respectively.

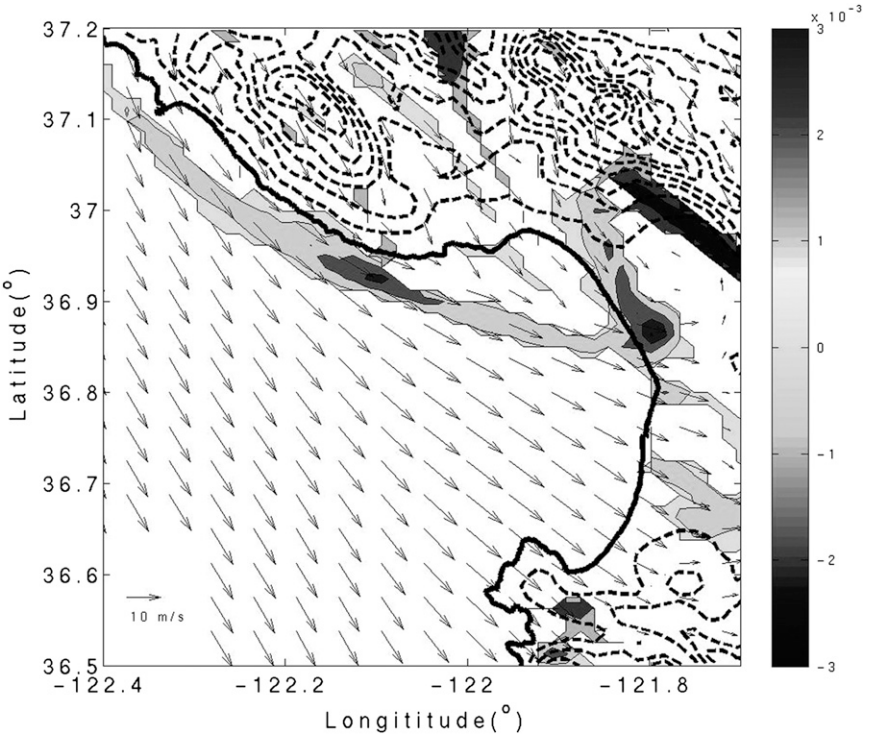

FIG. 10. The modeled 10-m wind field in the WRF-CLM superimposed over the shaded vertical vorticity (only the strength larger than $|5 \times 10^{-4}|$ s^{-1} is shown) at 1800 LST 13 Apr. The terrain is shown as the dashed contours (every 200 m is shown).

a few kilometers to the east. The sea breeze is responsible for the advection of vorticity created along the coast to the northwest of Santa Cruz, which is consistent with Archer and Jacobson (2005).

Figure 9b shows that the advection of vorticity by the sea breeze along the coast accumulates and then forms the SCE, which is initially limited to the area over the northeast part of Monterey Bay (near metrological station KWVI). Owing to the weakening of the sea breeze (the main constraint of SCE), the SCE is detached from northern Monterey Bay (Santa Cruz Mountains) and moves southeastward. The SCE then develops into a larger eddy that lasts until 0300 LST and has a horizontal size of approximately 100 km. Figure 9c shows the mature stage of the SCE. The wind vorticity inside the core of the SCE then weakens and dissipates before the SCE reaches land. After the SCE reaches land, it dissipates with a weak and variable wind field.

c. *UFW*

A persistent northerly wind (i.e., UFW) is commonly found along the California coast in spring and summer and may last for a few days. Figure 10 shows the 10-m wind and vorticity fields during a strong UFW at 1800 LST 13 April. This UFW is consistent with the meteorological observations in Fig. 4. A north-northwesterly wind outside the bay turns into a northwesterly flow inside the bay. The wind speed is lower inside the bay due to the terrain friction. The overall wind speed can be higher than 10 m s^{-1} (even above 15 m s^{-1} in some offshore areas). Compared to the typical SCE development as shown in Fig. 9, the vorticity location is farther east. The full SCE cannot form during the UFW because vorticity stays only on the northern coast of Monterey Bay and dissipates quickly. The modeled UFW is strong enough until 15 April to sweep away any attempt at SCE formation inside the bay. Note that, from the sea surface observations shown in Fig. 3b, the SST drops significantly during the UFW period. Unfortunately, this cannot be resolved in the WRF-CLM since the 6-hourly coarse-resolution NCEP–NCAR reanalysis SST forcing is imposed.

5. Improved results through oceanic feedbacks

a. *Marine atmospheric boundary layer dynamics in the I-RMS*

The results discussed in the previous section indicate that the high-resolution WRF-CLM reasonably captures

most of the regional-scale atmospheric patterns. Surface temperature gradients and advection can be resolved in the WRF-CLM. However, the SST is constrained by the 6-hourly, coarse-resolution NCEP–NCAR reanalysis data and underestimates the energy fluxes through the air–sea interface, increasing the model uncertainty of future projections for coastal regions. The influences of ocean dynamics and feedbacks from the I-RMS to the MABL are discussed in this section.

The nonhydrostatic MBARM has been used in this study. Based on the Clausius–Clapeyron equation, warmer SSTs may directly introduce more water vapor and moisture flux into the atmosphere, which with warming can also contain more water vapor. Figure 11 shows the comparison between the WRF-CLM and the I-RMS in terms of moisture flux and mixing ratio due to the 0.6°C enhancement of SSTs at 1200 LST 14 April. The moisture flux and water vapor play an important role in modulating the nearshore dynamics of the air–land–sea interactions. The prevailing UFW dominates during this time period and a strong sea breeze also occurs in Monterey Bay. During the UFW event, the prevailing northerly wind speed increases and can be higher than 15 m s^{-1} in both the observations and simulations. The surface temperature also drops significantly (see Figs. 3 and 4 and the associated discussion).

The 10-m wind fields are superimposed on the top panels in Fig. 11, which show relatively consistent wind patterns. Most of the submesoscale and air–land–sea patterns discussed in the previous sections are quite similar. This is expected since the differences result only from the energy flux through the SSTs. However, the wind strengths in these simulations are different, and small-scale features above the ocean are simulated only with the I-RMS. Figure 12 shows the detailed differences (I-RMS minus WRF-CLM) between the two model simulations of surface temperature, surface moisture flux, and the 10-m mixing ratio (water vapor). The 10-m wind difference between the I-RMS and WRF-CLM is superimposed on the 10-m temperature difference map (Fig. 12a). It is clear that the northerly wind is slightly enhanced in the I-RMS. The most significant differences occur above the ocean with a higher temperature, and two major regions with significant differences are identified throughout the numerical experiments. First of all, the surface moisture flux and water vapor increase significantly near the location where an oceanic anticyclonic warm eddy, discussed in detail later, is simulated by I-RMS, but not by WRF-CLM (Figs. 12b and 12c). Such moisture differences are directly advected downstream and are consistent with the increases in both the onshore moisture flux gradient and water vapor pressure, as shown in the right panels of Fig. 11. The other large difference is found across the mouth of Monterey Bay, which extends from the north of the bay and forms a filament. The enhanced moisture flux gradient may help the formation of the SCE. At noon, the SCE is initiated just north of Monterey Bay along the west ridge of the Coastal Mountains (Fig. 9), where the moisture flux gradient is significantly larger in the I-RMS. The vorticity generated in this area then forms the SCE. After the SCE is established, it may propagate into the center of the bay and persist for a few hours before disappearing. The dynamic processes in the I-RMS are similar to those in the WRF-CLM except for the strength and affected area. Both of these regions show significant differences and suggest that the vertical temperature gradient contributes mostly to the mixing ratio.

In the I-RMS, the influence of the improved SST simulations on the inland water vapor and air–land interaction is limited (Figs. 12a–c). The difference is mostly constrained above the ocean and advected downstream, as expected. This indicates that vertical and horizontal fluxes dominate the MABL. The surface moisture flux difference is mainly in the ocean, but the differences in surface temperature and 10-m mixing ratio are found in the Coastal Mountains and Salinas Valley. The temperature difference between the SSTs outside Monterey Bay is 0.4°C higher in the I-RMS than in the WRF-CLM and thus the MABL can contain more water vapor through latent heat flux. This result shows the significance of ocean impacts and moisture flux transported inland directly through atmospheric dynamics.

In general, the near-surface prevailing wind is slightly stronger in the I-RMS above the ocean; a large difference is seen outside Monterey Bay (approximately 1–1.5 m s^{-1}; see Fig. 12). The sea-breeze pattern inside the bay is also stronger in the I-RMS as compared to that in the WRF-CLM (not shown here). The maximum temperature difference occurs to the north of the core of the anticyclonic gyre outside of Monterey Bay. This may result from a warmer and nonuniform SST field in the I-RMS (not shown here), indicating greater nonuniformity of the ocean feedback on the MABL, which may cause further fog formation onshore in long-term climate integrations.

b. Ocean dynamics in the Integrated Regional Model System

The climatological wind stress used in the original MBARM is relatively uniform and mainly northwesterly outside Monterey Bay (Tseng et al. 2005). However, in the I-RMS, the high-resolution WRF-CLM wind field is used to force the nonhydrostatic coastal ocean model, which is the ocean component of the I-RMS (e.g., Figs. 8–10). The high-resolution wind field includes

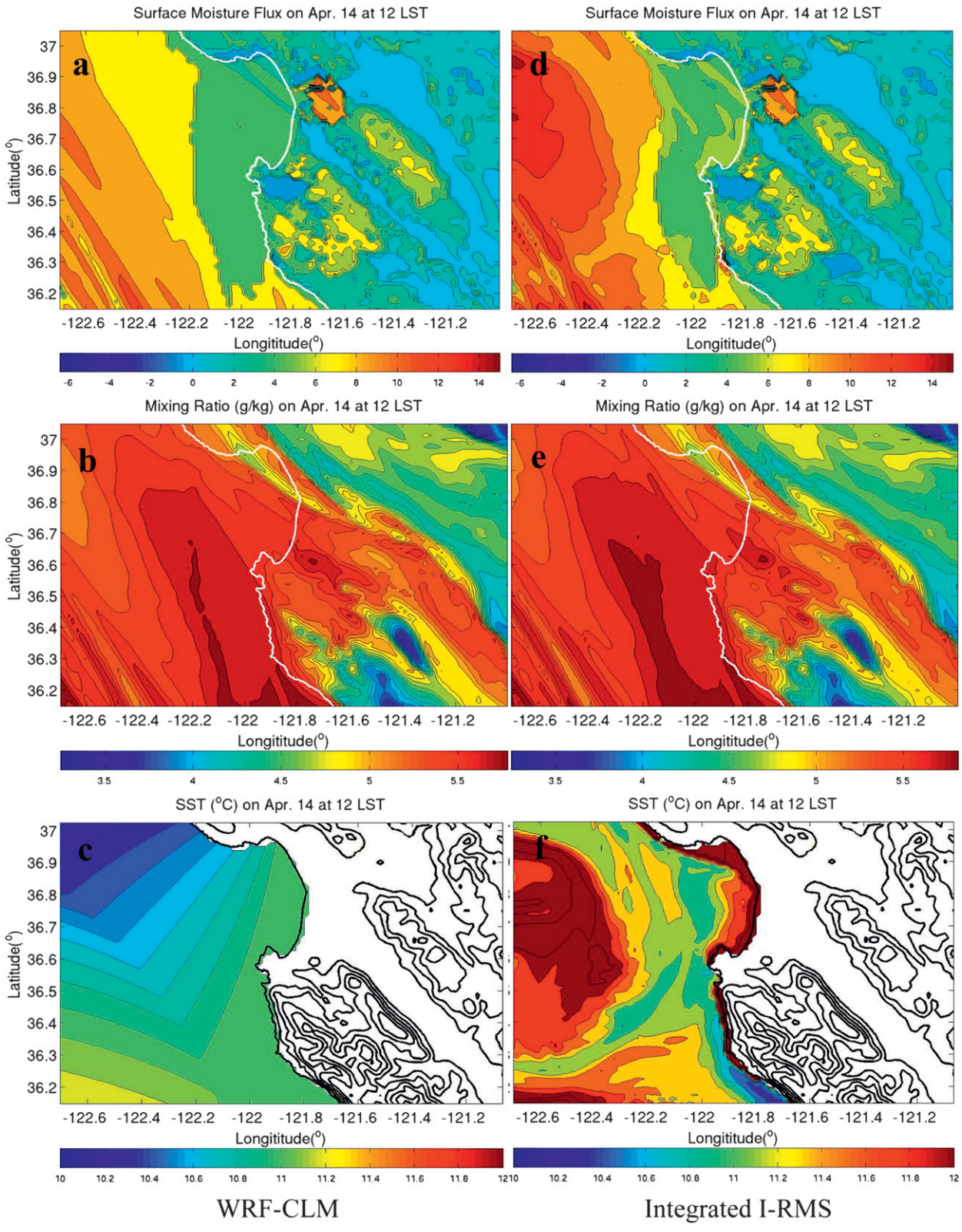

FIG. 11. The modeled (a) surface moisture flux, (b) 10-m mixing ratio, and (c) SST at 1200 LST 14 Apr in the WRF-CLM. (d)–(f) As in (a)–(c), but for the I-RMS.

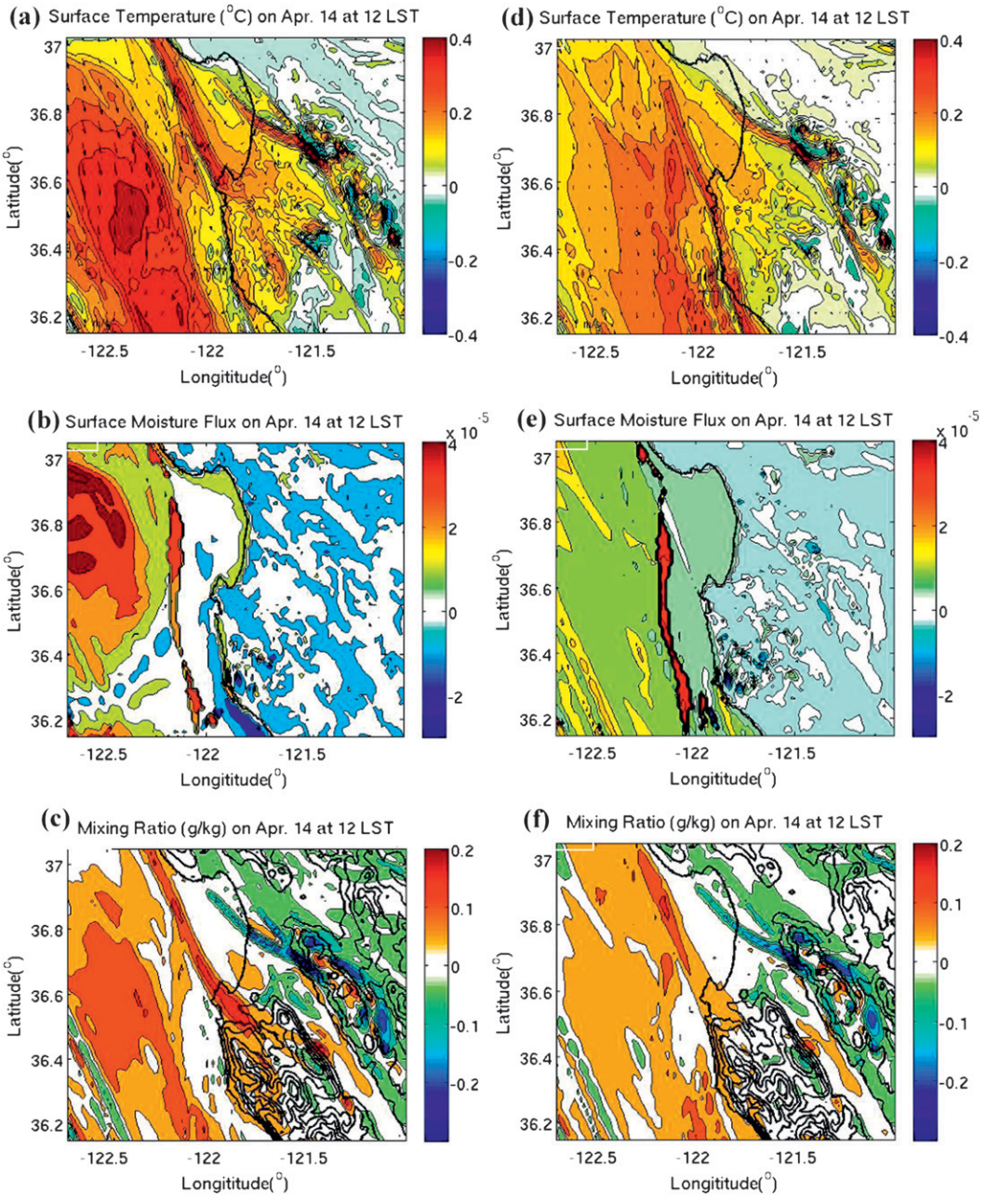

FIG. 12. The differences between the I-RMS and WRF-CLM at 1200 LST 14 Apr for (a) surface temperature, (b) surface moisture flux, and (c) 10-m mixing ratio (water vapor). The 10-m wind difference is superimposed on the 10-m temperature difference map (top). (d)–(f) As in (a)–(c), but for the difference between the WRF-CLM$_{plus}$ and WRF-CLM.

more realistic and detailed submesoscale features, such as the LSB and SCE. Since wind stress plays a dominant role in modulating the ocean surface and subsurface circulation, high-resolution wind stress triggers a near-surface ocean response and feedback to the MABL through the air–sea flux.

Here, we show the ocean response to different atmospheric wind forcings during the UFW period, and the interpolated climatological wind stress from Hellerman and Rosenstein (1983) as well as the high-resolution WRF-CLM wind stress, respectively. The UFW lasts for only a few days; therefore, this short-term event and its response to winds cannot be resolved using the climatologically forced wind. However, this feature is well resolved in the I-RMS and potentially feeds back into the MABL. Figure 13a shows the sea surface current

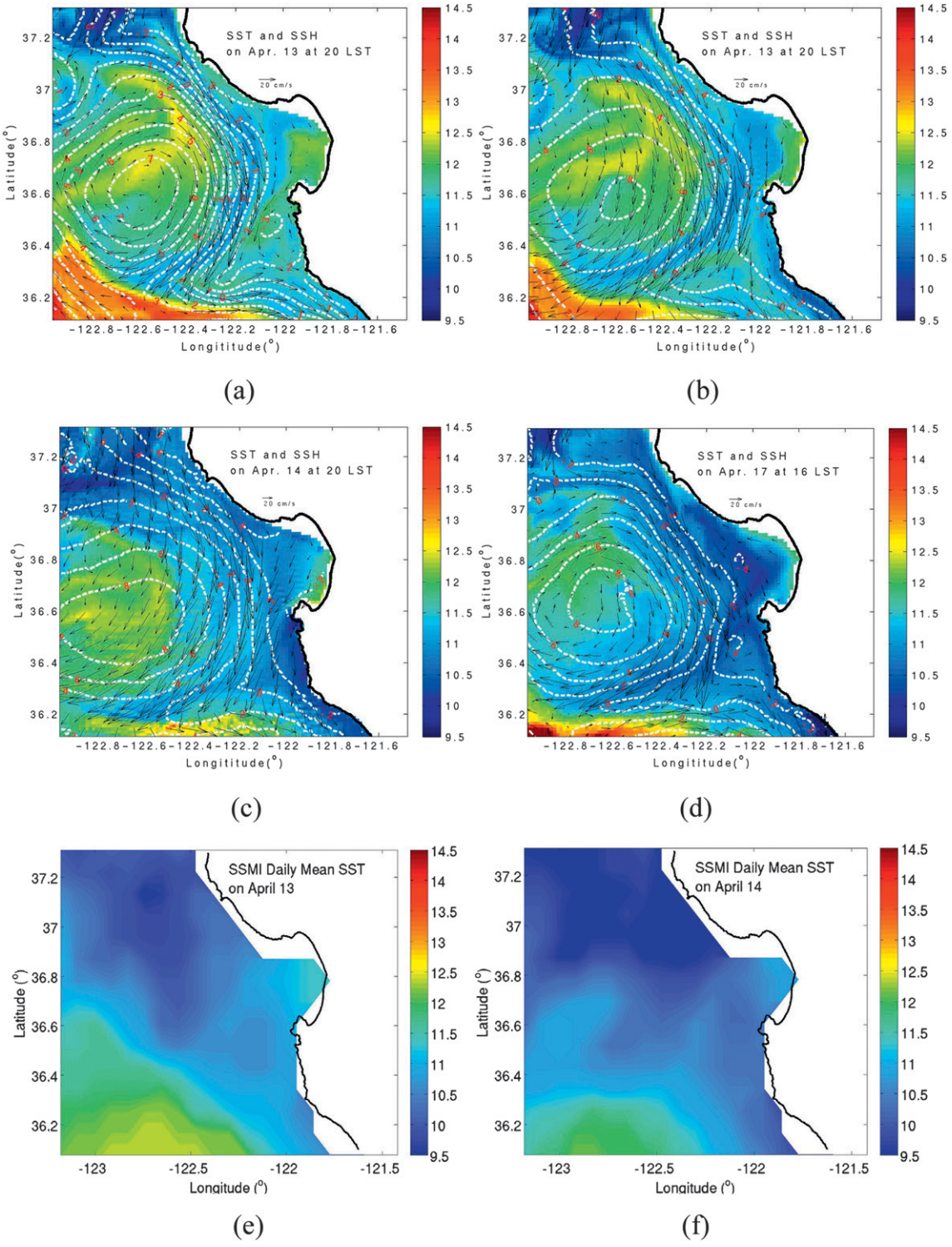

FIG. 13. The sea surface current fields superimposed over the equivalent sea surface height (SSH, white dashed contour line; unit is cm) and SST (color shaded) for the (a) climatological wind stress forcing run at 2000 LST 13 Apr, (b) I-RMS at 2000 LST 13 Apr (initialization of coastal upwelling), (c) I-RMS at 2000 LST 14 Apr (during the strong UFW), and (d) I-RMS at 1600 LST 17 Apr (upwelling relaxation period). (e) The observed daily average MW + IR optimally interpolated SST on 13 Apr. (f) As in (e), but 14 Apr.

fields superimposed over the equivalent sea surface height (SSH, white dashed contour line) and SST (color shaded) for the climatological wind stress forced run. Figure 13b shows the surface current fields at the same time based on the I-RMS. A large, warm anticyclonic gyre is seen in the wind climatology forced simulations, which are similar to the climatological observations (Tseng et al. 2005). The uniform and interpolated wind stress causes the surface circulation in MBARM to remain geostrophic, and thus the surface velocity field is approximately parallel to the SSH. However, an ageostrophic balance is clear in the I-RMS (Fig. 13b) due to the nonuniform and real-time momentum flux. The ageostrophic component is mainly due to the Ekman dynamics. The warm anticyclonic gyre in the SSH also intensifies, suggesting that its formation is consistent with the prevailing northwesterly wind with the ageostrophic adjustment. The weak, inshore poleward current in the Hellerman and Rosenstein (1983) wind-forced MBARM is almost reversed in the I-RMS. This is due to the enhanced UFW that began on 13 April. A stronger Ekman suction (upwelling) around 14–15 April is also observed in the I-RMS. With the updating of momentum flux every 200 s, the effect of a stronger UFW is well captured. Figure 13b shows the initial stage of the UFW event in the I-RMS (also see Fig. 4 for the observations). The UFW starts to enhance in the afternoon of 13 April. A few hours later, the ocean component of the I-RMS has been forced, and a significant Ekman transport is simulated in the surface current. The ageostrophic current not only causes the typical upwelling in Monterey Bay, but also transports cold water from north to south outside the bay. Cold upwelling is seen at the mouth of the bay and in the east of the warm anticyclonic gyre. This process lasts until 15 April.

Observations show that the temperature drops approximately 2°C (from 12° to 10°C) at station 46042 (M2; 36.8°N, 122.4°W) within 1 day. The I-RMS shows an approximate 1°–1.5°C temperature decrease in the nearby area. Figure 13c shows the surface current and the SST distribution 24 h later. The cooling process is found almost everywhere in the simulated area. Inside the bay, a 1°C temperature drop is found in the I-RMS. The offshore, warm anticyclonic gyre is also relaxed due to the upwelling. The cooling is also more evident in the two typical upwelling centers north and south of Monterey Bay due to topographical enhancement (Tseng et al. 2005).

Figure 13d shows the surface pattern and SST distribution during the relaxation period in the I-RMS on 17 April. The pressure gradient, Coriolis force, and surface current tended to reach geostrophic balance 3 days after the strong UFW event. However, the SST in the I-RMS was still 0.5°–1°C cooler. The SSH shows that the magnitude of the anticyclonic gyre outside Monterey Bay in the I-RMS is slightly larger than that in the Hellerman and Rosenstein (1983) wind-forced MBARM (not shown here), showing a slightly stronger gyre. This is expected since finescale detailed forcing is imposed in the I-RMS. Note that long-term regional climate integrations may have a remarkable effect on the heat flux and momentum flux in the Monterey Bay area, since coastal upwelling occurs frequently in spring and summer along the West Coast of the United States, which can be seen as the most important contribution of the I-RMS.

Figures 13e and 13f further show the observed daily average microwave (MW) + infrared (IR) optimally interpolated SSTs for the same regions on 13 and 14 April, respectively. The resolution is approximately 9 km (downloadable online at http://www.ssmi.com). Note that strong upwelling occurs near Point Año Nuevo on 13 April and is consistent with the model results (Figs. 13a and 13b). The cold water then propagates equatorward across the bay mouth and moves to the other strong upwelling center south of the bay due to the strong UFW. In general, the model reproduces this important dynamic of the upwelling that is observed in the remotely sensed SST observations. The model results provide more detailed spatial and temporal structures. However, the observational resolution is too coarse to fully resolve upwelling filaments and finescale coastal structures across the bay mouth (Tseng et al. 2005).

6. Sensitivity of SST forcing on the WRF-CLM

The major feedback of ocean dynamics on the I-RMS is the modeled SST. Better representation of the SST spatial distribution will better constrain the model dynamics and long-term integration. However, some uncertainty remains. To further explore the sensitivity of SST forcing on the WRF-CLM, an analysis of difference fields between the WRF-CLM$_{plus}$ (which imposes a 0.6°C uniformly higher SST on the WRF-CLM) and the WRF-CLM at 1200 LST 14 April is shown in Fig. 12, where Fig. 12d is the surface temperature difference (superimposed over the 10-m wind difference between the WRF-CLM$_{plus}$ and the WRF-CLM), Fig.12e is the surface moisture flux difference, and Fig. 12f is the 10-m mixing ratio difference. Note that the area with significant differences is similar to that between the I-RMS and the WRF-CLM (Figs. 12a–c). However, the magnitudes differ. When the surface moisture flux is increased, the warm gyre is completely missing and the extended filament region associated with the SCE weakens. The surface temperature and the 10-m mixing ratio above the ocean are also enhanced, with these differences transported inland. In particular, it is seen that a significantly reduced mixing ratio is found in the mountainous

areas east of the Salinas Valley, implying a reduction in water vapor and fog formation (similar to Figs. 12a–c). The difference pattern in Figs. 12d–f is more uniform than that in the I-RMS above the offshore ocean in Fig. 12a–c (e.g., missing the warm ocean eddy feature). The main enhancement of the wind field may be due to the increase in the southward pressure gradient outside of the Monterey Bay, resulting from the higher SST (such as the warm core) and lower SLP. This enhances the propagation of temperature and other variable and flux differences downstream. The sensitivity test concludes that the nonuniform 0.6°C SST distribution difference and temperature convection contribute to the water budget of the MABL thermodynamically. Also, atmospheric dynamics play an important role in transporting ocean influences farther inland.

7. Conclusions

The coupled I-RMS for the California coast is developed and evaluated in this study. Ocean dynamics and feedbacks are taken into account, resulting in better simulations of air–land–sea interactions near the West Coast of the United States. The improvements in our modeling results provide a more accurate representation of atmospheric processes at local to regional scales. The improved simulations result in a better understating of nearshore processes in the MABL.

Key submesoscale processes resulting from air–land–sea interactions are examined for 11–20 April 2009. These processes include the LSB, SCE, and coastal upwelling. The effects of ocean feedbacks on the MABL are also evaluated. Observations and WRF-CLM and I-RMS simulations all indicate that a typical land breeze sometimes occurs in the early morning. However, a sea breeze is seen to occur almost every afternoon during our study period. A unique cyclonic vortex, the SCE, is found inside Monterey Bay nearly every night. Such a vortex commonly lasts for 4–6 h and has a horizontal scale of 100 km in the mature stage. These phenomena occur at a daily temporal scale, but none of them are resolved or parameterized in current AOGCMs. Moreover, the observations indicate a strong UFW occurring from 13 to 15 April. Such a strong UFW reproduced by I-RMS results in a 2°C SST decrease in the vicinity of the mouth of Monterey Bay and a 1.5°C SST decrease inside the bay. These simulated SST decreases are well explained by the upwelling processes due to the UFW.

The I-RMS shows that including finescale ocean dynamics may modulate the water budgets in the MABL through the energy flux at the air–sea interface. Similar to the observation (e.g., M2 mooring), the typical upwelling process is well captured and simulated with the I-RMS, which could reduce the SSTs by 1°–1.5°C. This is associated with an ageostrophic adjustment in the upper ocean. The nonuniform SSTs due to the coastal upwelling may further enhance fog formation inshore in a long-term climate integration. The sensitivity of SSTs in the WRF-CLM shows that increasing SSTs uniformly (in this case, 0.6°C) introduces a stronger thermal low at the southern part of Monterey Bay and thus enhances the northerly prevailing wind outside the bay. The ocean influences are transported directly inland through atmospheric dynamics. Further study of long-term climate integration impacts will be investigated in a future study.

Acknowledgments. The financial support from National Science Council, Taiwan (Grants 992811M002107, 1002628M002010MY2, and 1002199M001029MY5: Laboratory for Climate Change Research-Consortium for Climate Change Study), is appreciated. We acknowledge the data provided by the governmental agencies, commercial firms, and educational institutions participating in MesoWest. We would also like to acknowledge the National Center for High-Performance Computing, Taiwan, for providing computing resources to facilitate this research. Detailed comments from three anonymous reviewers are deeply appreciated.

REFERENCES

Archer, C. L., and M. Z. Jacobson, 2005: The Santa Cruz eddy. Part II: Mechanisms of formation. *Mon. Wea. Rev.,* **133,** 2387–2405.

——, ——, and F. L. Ludwig, 2005: The Santa Cruz eddy. Part I: Observation and statistics. *Mon. Wea. Rev.,* **133,** 767–782.

Atkinson, B. W., 1981: *Mesoscale Atmospheric Circulations*. Academic Press, 495 pp.

Banta, R. M., 1995: Sea breezes shallow and deep on the California coast. *Mon. Wea. Rev.,* **123,** 3614–3622.

Breaker, L. C., and C. N. K. Mooers, 1986: Oceanic variability off the central California coast. *Prog. Oceanogr.,* **17,** 61–135.

Cui, Z., M. Tjernstrom, and B. Grisogono, 1998: Idealized simulations of atmospheric coastal flow along the central coast of California. *J. Appl. Meteor.,* **37,** 1332–1363.

Dorman, C. E., and C. D. Winant, 2000: The structure and variability of the marine atmosphere around the Santa Barbara Channel. *Mon. Wea. Rev.,* **128,** 261–282.

Harvey, N., and R. Nicholls, 2008: Global sea-level rise and coastal vulnerability. *Sustain. Sci.,* **3,** 5–7.

Haurwitz, B., 1947: Comments on the sea-breeze circulation. *J. Meteor.,* **4,** 1–8.

Hellerman, S., and M. Rosenstein, 1983: Normal monthly wind stress over the world ocean with error estimates. *J. Phys. Oceanogr.,* **13,** 1093–1104.

Huyer, A., 1983: Coastal upwelling in the California current system. *Prog. Oceanogr.,* **12,** 259–284.

Jin, J., N. L. Miller, and N. J. Schlegel, 2010: Sensitivity study of four land-surface schemes in the Weather Research and Forecasting (WRF) model. *Adv. Meteor.,* **2010,** doi:10.1155/2010/167436.

Johnstone, J., and T. Dawson, 2010: Climatic context and ecological implications of summer fog decline in the coast redwood region. *Proc. Natl. Acad. Sci. USA,* **107,** 4533–4538.

Kistler, R., and Coauthors, 2001: The NCEP–NCAR 50-Year Reanalysis: Monthly means CD-ROM and documentation. *Bull. Amer. Meteor. Soc.,* **82,** 247–267.

Large, W. G., and G. Danabasoglu, 2006: Attribution and impacts of upper ocean biases in CCSM3. *J. Climate,* **19,** 2325–2346.

Lyons, W. A., 1972: The climatology and prediction of the Chicago lake breeze. *J. Appl. Meteor.,* **11,** 1259–1270.

McGranahan, G., D. Balk, and B. Anderson, 2007: The rising tide: Assessing the risks of climate change and human settlements in low elevation coastal zones. *Environ. Urban.,* **19,** 17–37.

Miller, N. L., and Coauthors, 2009: An analysis of simulated California climate using multiple dynamical and statistical techniques. CEC-500-2009-017-F, California Energy Commission, 35 pp.

Oleson, K. W., and Coauthors, 2004: Technical description of the Community Land Model version 3.0 (CLM). NCAR Tech. Note NCAR-TN-451+STR.

Skamarock, W. C., and J. B. Klemp, 2008: A time-split nonhydrostatic atmospheric model for weather research and forecasting applications. *J. Comput. Phys.,* **227,** 3465–3485.

——, ——, J. Dudhia, D. Gill, D. Barker, W. Wang, and J. G. Powers, 2005: A description of the advanced research WRF version 2. NCAR Tech. Note NCAR/TN-468+STR, 88 pp.

Smith, N., 1981: An investigation of seasonal upwelling along the Atlantic coast of Florida. *Ecohydrodynamics,* J. C. J. Nihoul, Ed., Elsevier, 79–98.

Solomon, S., D. Qin, M. Manning, M. Marquis, K. Averyt, M. M. B. Tignor, H. L. Miller Jr., and Z. Chen, Eds., 2007: *Climate Change 2007: The Physical Science Basis*. Cambridge University Press, 996 pp.

Stewart, R. H., 2008: *Introduction to Physical Oceanography*. Department of Oceanography, Texas A&M University, 344 pp.

Tseng, Y. H., and J. H. Ferziger, 2001a: Effects of coastal geometry and the formation of cyclonic/anti-cyclonic eddies on turbulent mixing in upwelling simulation. *J. Turbul.,* **2,** doi:10.1088/1468-5248/2/1/014.

——, and ——, 2001b: Mixing and available potential energy in stratified flows. *Phys. Fluids,* **13,** 1281–1293.

——, and L. C. Breaker, 2007: Nonhydrostatic simulation of the regional circulation in the Monterey Bay area. *J. Geophys. Res.,* **112,** C12017, doi:10.1029/2007JC004093.

——, D. E. Dietrich, and J. H. Ferziger, 2005: Regional circulation of the Monterey Bay region—Hydrostatic versus non-hydrostatic modeling. *J. Geophys. Res.,* **110,** C09015, doi:10.1029/2003JC002153.

Vesecky, J. F., C. C. Teague, R. G. Onstott, J. M. Daida, P. E. Hansen, D. Fernandez, N. G. Schnepf, and K. W. Fischer, 1997: Surface current response to land–sea breeze circulation in Monterey Bay, California as observed by a new multifrequency HF radar. *Proc. 1997 Int. Geoscience and Remote Sensing Symp.,* Singapore, IEEE, H03.04.1–H03.04.3.

Wong F. L., and S. E. Eittreim, 2001: Continental shelf GIS for the Monterey Bay National Marine Sanctuary. U.S. Geological Survey Open File Rep. 01-179.